

Structure of the $\Lambda(1405)$ and the $K^-d \rightarrow \pi\Sigma n$ reaction

Shota Ohnishi,^{1,*} Yoichi Ikeda,² Tetsuo Hyodo,³ and Wolfram Weise^{4,5}

¹*Department of Physics, Hokkaido University, Sapporo 060-0810, Japan*

²*RIKEN Nishina Center, Wako, Saitama 351-0198, Japan*

³*Yukawa Institute for Theoretical Physics, Kyoto University, Kyoto 606-8502, Japan*

⁴*ECT*, Villa Tambosi, I-38123 Villazzano (Trento), Italy*

⁵*Physik Department, Technische Universität München, D-85747 Garching, Germany*

(Dated: October 11, 2018)

The $\Lambda(1405)$ resonance production reaction is investigated within the framework of the coupled-channels Alt-Grassberger-Sandhas (AGS) equations. We perform full three-body calculations for the $\bar{K}NN$ - πYN amplitudes on the physical real energy axis and investigate how the signature of the $\Lambda(1405)$ appears in the cross sections of the $K^-d \rightarrow \pi\Sigma n$ reactions, also in view of the planned E31 experiment at J-PARC. Two types of meson-baryon interaction models are considered: an energy-dependent interaction based on chiral $SU(3)$ effective field theory, and an energy-independent version that has been used repeatedly in phenomenological approaches. These two models have different off-shell properties that imply correspondingly different behavior in the three-body system. We investigate how these features show up in differential cross sections of $K^-d \rightarrow \pi\Sigma n$ reactions. Characteristic patterns distinguishing between the two models are found in the invariant mass spectrum of the final $\pi\Sigma$ state. The $K^-d \rightarrow \pi\Sigma n$ reaction, with different $(\pi^\pm\Sigma^\mp$ and $\pi^0\Sigma^0)$ charge combinations in the final state, is thus demonstrated to be a useful tool for investigating the subthreshold behavior of the $\bar{K}N$ interaction.

PACS numbers: 14.20.Pt, 13.75.Jz, 21.85.+d, 25.80.Nv

I. INTRODUCTION

Understanding the structure of the $\Lambda(1405)$ is a long-standing issue in hadron physics. The nominal location of the $\Lambda(1405)$ mass, 27 MeV below the K^-p threshold, deviates prominently from the expected naive quark model pattern and indicates a more complex structure. Following early work by Dalitz *et al.* more than half a century ago [1, 2], the $\Lambda(1405)$ began to be considered as a quasi-bound $\bar{K}N$ state embedded in the $\pi\Sigma$ continuum. Motivated by such a picture, phenomenological $\bar{K}N$ potential models were designed to reproduce the $\Lambda(1405)$ mass together with two-body scattering data [3, 4].

A more systematic framework emerged with developments of meson-baryon effective field theory based on the spontaneous breaking of chiral $SU(3)_L \times SU(3)_R$ symmetry in low-energy QCD. In this theory the kaon is part of the pseudoscalar octet of Nambu-Goldstone bosons, but with an important explicit chiral symmetry breaking term introduced by its mass, $m_K \sim 0.5$ GeV, that reflects the relatively large mass of the strange quark, $m_s \sim 0.1$ GeV. Over the years, chiral $SU(3)$ dynamics, as the synthesis of chiral effective field theory and coupled channels methods [5–8], has turned out to be a highly successful approach to deal with $\bar{K}N$ interactions and the $\Lambda(1405)$.

Even though the phenomenological and the chiral $SU(3)$ $\bar{K}N$ interactions produce comparable results at and above $\bar{K}N$ threshold, they differ significantly in their extrapolations to subthreshold energies [9]. The phenomenological $\bar{K}N$ interactions are constructed to

describe the $\Lambda(1405)$ as a single pole of the scattering amplitude around 1405 MeV, corresponding to a quasi-bound state of the $\bar{K}N$ system with a binding energy of about 30 MeV. On the other hand, the $\bar{K}N$ - $\pi\Sigma$ coupled-channels amplitude resulting from chiral $SU(3)$ dynamics has two poles, one of which is located around 1420 MeV [7, 10] while the other pole represents a broad structure above the $\pi\Sigma$ threshold. The pole at 1420 (rather than 1405) MeV corresponds to a $\bar{K}N$ quasi-bound system with a binding energy of 15 MeV, about half the binding produced with the purely phenomenological $\bar{K}N$ potentials. These differences in the pole structures come from different off-shell properties. The $\bar{K}N$ interaction based on chiral $SU(3)$ dynamics is necessarily energy-dependent: the Nambu-Goldstone boson nature of the \bar{K} dictates that the leading-order $\bar{K}N$ s -wave interaction is proportional to the time derivative of the antikaon field and thus varies linearly with the \bar{K} energy. Consequently, as one extrapolates deeper into the subthreshold region, the attraction generated by this interaction becomes progressively weaker than the one proposed by the energy-independent phenomenological potentials. At the same time, corresponding differences occur in the strong $\bar{K}N \leftrightarrow \pi\Sigma$ channel couplings.

Hence the $\bar{K}N$ binding energies predicted by interactions based on chiral $SU(3)$ dynamics are systematically smaller than those suggested by the phenomenological models. These differences are further enhanced in the so-called few-body kaonic nuclei, such as the strange dibaryon resonance under discussion in the $\bar{K}NN$ - πYN coupled system [11–21]. How a possible signature of this strange dibaryon resonance shows up in a suitable production reaction is of great interest as it reflects the two-body dynamics in the $\Lambda(1405)$ channel [22].

* s_ohnishi@nucl.sci.hokudai.ac.jp

Exploring the structure of the $\Lambda(1405)$ requires a precise determination of the $\bar{K}N$ - $\pi\Sigma$ interaction. The data base available to constrain these interactions includes the old K^-p scattering cross sections [23–27], the $\bar{K}N$ threshold branching ratios [28, 29], and the kaonic hydrogen measurements [30–32] with special emphasis on more recent accurate SIDDHARTA data [33, 34]. These latter data strongly constrain the $\bar{K}N$ input, as shown by the systematic study of chiral $SU(3)$ dynamics using next-to-leading order driving interactions [35, 36]. The experimental data just mentioned are collected at and above the $\bar{K}N$ threshold. Since $\pi\Sigma$ elastic scattering cannot be performed, the subthreshold energy region is only accessible by measuring mass spectra of decay products in reactions producing the $\Lambda(1405)$. The relevant $\pi\Sigma$ spectra have recently been measured in photoproduction reactions by the LEPS Collaboration at SPring-8 [37, 38] and by the CLAS Collaboration at JLab [39, 40], and in pp collisions by the HADES Collaboration at GSI [41]. The importance of accurately determined $\pi\Sigma$ spectra as constraints for the subthreshold $\bar{K}N$ interaction has also been emphasized in Refs. [42–45].

Yet another process of prime interest is the $K^-d \rightarrow \pi\Sigma n$ reaction. It was studied long ago by Braun *et al.* [46] in a bubble-chamber experiment at K^- momenta between 686 and 844 MeV. A new experiment is ongoing at J-PARC (E31 [47]) with a 1 GeV K^- beam¹. In the E31 experiment, the $\pi\Sigma$ production cross sections will be measured separately for all combinations of charges, i.e., $\pi^+\Sigma^-$, $\pi^-\Sigma^+$, and $\pi^0\Sigma^0$. It is therefore important to establish a theoretical framework for a detailed analysis of this reaction. Theoretical investigations of $K^-d \rightarrow \pi\Sigma n$ with comparable kinematics have previously been performed in simplified models assuming a two-step process [48–51]. To extract the information of the subthreshold $\bar{K}N$ interaction from the experimental spectrum, an improved framework for the reaction mechanism is called for.

In this work a full three-body calculation of the $\bar{K}NN$ - πYN amplitude is performed employing the coupled-channels Alt-Grassberger-Sandhas (AGS) equations. We investigate how the $\Lambda(1405)$ resonance manifests itself in the differential cross section of the $K^-d \rightarrow \pi\Sigma n$ reaction. At J-PARC it is planned to observe the $\Lambda(1405)$ in the $\pi\Sigma$ mass spectrum measured by detecting the forward kicked-out neutron [47]. Our calculation focuses on this observable. One of the aims is to study the role of different off-shell properties of the underlying interactions as they are realized in chiral $SU(3)$ dynamics versus phenomenological potential models. We thus employ two different types of $\bar{K}N$ - $\pi\Sigma$ interactions, i.e., energy-dependent (E-dep.) and energy-independent (E-indep.),

and examine how the different off-shell properties of these interactions show up in the three-body dynamics.

In Sec. II, we introduce the AGS equations for the three-body $\bar{K}NN$ - πYN system and derive the cross section for the $K^-d \rightarrow \pi\Sigma n$ reaction. The two-body interactions used in this work are summarized in Sec. III. The numerically computed differential cross sections are presented and discussed in Sec. IV. A summary follows in Sec. V.

II. THREE-BODY EQUATIONS

A. Alt-Grassberger-Sandhas equations for the $K^-d \rightarrow \pi\Sigma n$ reaction

We begin by constructing the three-body amplitudes relevant to the $K^-d \rightarrow \pi\Sigma n$ reaction. Throughout this paper it is assumed that the three-body processes take place via separable two-body interactions given by the following forms in the two-body center-of-mass (c.m.) frame:

$$V_{\alpha\beta}^{(I)}(\mathbf{q}'_i, \mathbf{q}_i; E) = g_{\alpha}^{*(I)}(\mathbf{q}'_i) \lambda_{\alpha\beta}^{(I)}(E) g_{\beta}^{(I)}(\mathbf{q}_i), \quad (1)$$

where $g_{\alpha}^{(I)}(\mathbf{q}_i)$ is a vertex (cutoff) factor of the two-body channel α with relative momentum \mathbf{q}_i and isospin I . The interaction matrix $\lambda_{\alpha\beta}^{(I)}(E)$ is a function of the total energy E in the two-body system. In the three-body system, we define the two-body energy as $E = \sqrt{(W - E_i(\mathbf{p}_i))^2 - p_i^2}$ with the three-body energy W and the spectator particle energy $E_i(\mathbf{p}_i)$, where \mathbf{p}_i is the relative momentum of the spectator particle i . The explicit forms of the relevant two-body interactions are presented in detail in Sec. III.

The ansatz (1) specifies strongly interacting two-body subsystems in the three-body processes. We refer to these meson-baryon or dibaryon subsystems conveniently as “isobars”. The three-body dynamics can then be described as quasi-two-body scattering of an isobar and a spectator particle in all possible coupled isobar-spectator channels. The quasi-two-body amplitudes, $X_{\alpha\beta}^{(I)(I')}(\mathbf{p}_i, \mathbf{p}_j; W)$, are determined by solving the AGS equations [52, 53],

$$\begin{aligned} X_{\alpha\beta}^{(I)(I')}(\mathbf{p}_i, \mathbf{p}_j, W) &= (1 - \delta_{ij}) Z_{\alpha\beta}^{(I)(I')}(\mathbf{p}_i, \mathbf{p}_j, W) \\ &+ \sum_{\gamma, \delta} \sum_{I''} \sum_{n \neq i} \int d^3 \mathbf{p}_n Z_{\alpha\gamma}^{(I)(I'')}(\mathbf{p}_i, \mathbf{p}_n, W) \\ &\times \tau_{\gamma\delta}^{(I'')}(W - E_n(\mathbf{p}_n), \mathbf{p}_n) X_{\delta\beta}^{(I'')(I')}(\mathbf{p}_n, \mathbf{p}_j, W). \end{aligned} \quad (2)$$

Here, α and β denote two-particle subsystems forming “isobars” with isospins I and I' , respectively; the subscripts i, j, n represent the spectator particles which include, respectively, N , Σ , Λ , \bar{K} , or π . The notations for

¹ In this paper, we focus on the in-flight reactions with relatively energetic incident kaons. The same $K^-d \rightarrow \pi\Sigma n$ process at lower energy has been studied in Ref. [61]. For theoretical studies with this kinematics, see Refs. [62, 63].

TABLE I. Indices specifying the two-body subsystems (“isobars”). Symbols Y denote hyperons Λ and Σ . The isospins in parentheses are allowed for $Y = \Sigma$. Mass splittings in the isospin multiplets are neglected.

Isobar	Allowed isospin(s)	Spectator particle	Three-body Fock space
$Y_K = \bar{K}_3 N_2, \bar{K}_3 N_1$	0, 1	N_1, N_2	$ N_1 N_2 \bar{K}_3\rangle$
$Y_\pi = \pi_3 Y_2, \pi_3 Y_1$	(0), 1	N_1, N_2	$ N_1 Y_2 \pi_3\rangle, Y_1 N_2 \pi_3\rangle$
$d = N_1 N_2$	0	\bar{K}_3	$ N_1 N_2 \bar{K}_3\rangle$
$N^* = \pi_3 N_2, \pi_3 N_1$	1/2, (3/2)	Y_1, Y_2	$ Y_1 N_2 \pi_3\rangle, N_1 Y_2 \pi_3\rangle$
$d_y = Y_1 N_2, Y_2 N_1$	1/2, (3/2)	π_3	$ Y_1 N_2 \pi_3\rangle, N_1 Y_2 \pi_3\rangle$

the isobars are summarized in Table I. As pointed out in Sec. III, in this work we include only the 3S_1 partial wave for the NN interaction, thus only the isospin $I = 0$ state appears for the NN subsystem (the isobar denoted d). For later purposes the partial wave projections of the amplitudes X of Eq. (2) are needed. They are given as:

written as:

$$\begin{aligned}
X_{\alpha\beta,L}^{(I)(I')}(p_i, p_j, W) &= (1 - \delta_{ij}) Z_{\alpha\beta,L}^{(I)(I')}(p_i, p_j, W) \\
&+ \sum_{\gamma,\delta} \sum_{I''} \sum_{n \neq i} \int dp_n p_n^2 Z_{\alpha\gamma,L}^{(I)(I'')}(p_i, p_n, W) \\
&\times \tau_{\gamma\delta}^{(I'')}(W - E_n(\mathbf{p}_n), \mathbf{p}_n) X_{\delta\beta,L}^{(I'')(I')}(p_n, p_j, W). \quad (4)
\end{aligned}$$

The driving term $Z_{\alpha\beta}^{(I)(I')}(\mathbf{p}_i, \mathbf{p}_j; W)$ describes a particle-exchange interaction process connecting two-body channels, $\beta \rightarrow \alpha$, and corresponding spectators as illustrated in Fig. 1(a). It is given by:

$$\begin{aligned}
X_{\alpha\beta,L}^{(I)(I')}(p_i, p_j; W) &= \frac{1}{2} \int_{-1}^1 d\cos\theta X_{\alpha\beta}^{(I)(I')}(\mathbf{p}_i, \mathbf{p}_j; W) P_L(\cos\theta) \quad (3) \\
Z_{\alpha\beta}^{(I)(I')}(\mathbf{p}_i, \mathbf{p}_j; W) &= \frac{g_\alpha^{(I)}(\mathbf{q}_i) g_\beta^{*(I')}(\mathbf{q}_j)}{W - E_i(\mathbf{p}_i) - E_j(\mathbf{p}_j) - E_k(\mathbf{p}_k) + i\epsilon}, \quad (5)
\end{aligned}$$

where $E_i(\mathbf{p}_i)$ and $E_j(\mathbf{p}_j)$ are the energies of the spectator particles i and j , respectively; $E_k(\mathbf{p}_k)$ with $\mathbf{p}_k = -\mathbf{p}_i - \mathbf{p}_j$ is the energy of the exchanged particle k ; \mathbf{q}_i (\mathbf{q}_j) is the relative momentum between the exchange-particle and the spectator-particle j (i). Using relativistic kinematics we have $E_n(\mathbf{p}_n) = \sqrt{m_n^2 + \mathbf{p}_n^2}$ ($n = i, j, k$) and $q_i = |\mathbf{q}_i|$ is defined as

$$q_i = \sqrt{\left(\frac{M_{jk}^2 + m_j^2 - m_k^2}{2M_{jk}}\right)^2 - m_j^2}, \quad (6)$$

$$\begin{aligned}
M_{jk}(\mathbf{q}_i) &= \sqrt{(E_j(\mathbf{p}_j) + E_k(\mathbf{p}_k))^2 - \mathbf{p}_i^2} \\
&= E_j(\mathbf{q}_i) + E_k(\mathbf{q}_i). \quad (7)
\end{aligned}$$

with $\cos\theta = \hat{\mathbf{p}}_i \cdot \hat{\mathbf{p}}_j$ and the notation $\hat{\mathbf{p}} \equiv \mathbf{p}/|\mathbf{p}|$. Here, P_L is the Legendre polynomial with orbital angular momentum L between isobar and spectator particle. After the partial wave projections the AGS equations (2) are

The isobar amplitudes, $\tau_{\alpha\beta}^{(I)}(W - E_i(\mathbf{p}_i), \mathbf{p}_i)$ as illustrated in Fig. 1 (b), are determined by solving the Lippmann-Schwinger equations with the two-body interaction (1),

$$\tau_{\alpha\beta}^{(I)}(W - E_i(\mathbf{p}_i), \mathbf{p}_i) = \lambda_{\alpha\beta}^{(I)} + \sum_{\gamma} \int dq_i q_i^2 \frac{\lambda_{\alpha\gamma}^{(I)} |g_\gamma^{(I)}(q_i)|^2}{W - E_i(\mathbf{p}_i) - E_{jk}(\mathbf{p}_i, \mathbf{q}_i)} \tau_{\gamma\beta}^{(I)}(W - E_i(\mathbf{p}_i), \mathbf{p}_i). \quad (8)$$

Here, $E_{jk}(\mathbf{p}_i, \mathbf{q}_i)$ is the energy of the interacting pair (jk), $E_{jk}(\mathbf{p}_i, \mathbf{q}_i) = \sqrt{M_{jk}^2(\mathbf{q}_i) + \mathbf{p}_i^2}$.

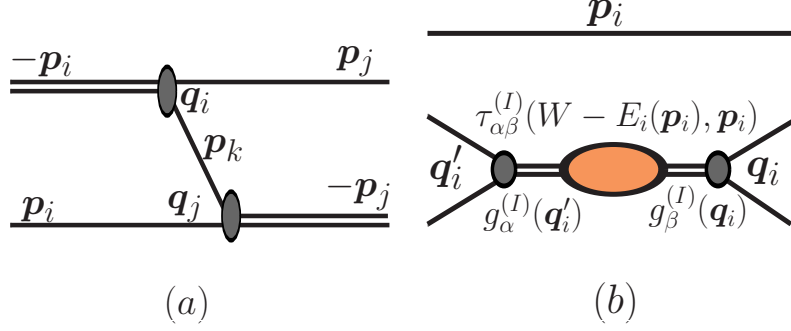


FIG. 1. (a) One particle exchange interaction $Z_{\alpha\beta,L}^{(I)(I')}(p_i, p_j, W)$. (b) Isobar propagator $\tau_{\alpha\beta}^{(I)}(W - E_i(\mathbf{p}_i), \mathbf{p}_i)$.

After antisymmetrization of the two-nucleon states in the three-body system, the coupled-channels AGS matrix integral equations (4) are written formally and symbolically (suppressing sums, integrals and all indices other than the isobar assignments) as:

$$\begin{pmatrix} X_{Y_K d} \\ X_{Y_\pi d} \\ X_{dd} \\ X_{N^* d} \\ X_{d_y d} \end{pmatrix} = \begin{pmatrix} 2Z_{Y_K d} \\ 0 \\ 0 \\ 0 \\ 0 \end{pmatrix} - \begin{pmatrix} Z_{Y_K Y_K} \tau_{Y_K Y_K} & Z_{Y_K Y_K} \tau_{Y_K Y_\pi} & 2Z_{Y_K d} \tau_{dd} & 0 & 0 \\ 0 & 0 & 0 & Z_{Y_\pi N^*} \tau_{N^* N^*} & Z_{Y_\pi d_y} \tau_{d_y d_y} \\ Z_{d Y_K} \tau_{Y_K Y_K} & Z_{d Y_K} \tau_{Y_K Y_\pi} & 0 & 0 & 0 \\ Z_{N^* Y_\pi} \tau_{Y_\pi Y_K} & Z_{N^* Y_\pi} \tau_{Y_\pi Y_\pi} & 0 & 0 & Z_{N^* d_y} \tau_{d_y d_y} \\ Z_{d_y Y_\pi} \tau_{Y_\pi Y_K} & Z_{d_y Y_\pi} \tau_{Y_\pi Y_\pi} & 0 & Z_{d_y N^*} \tau_{N^* N^*} & 0 \end{pmatrix} \begin{pmatrix} X_{Y_K d} \\ X_{Y_\pi d} \\ X_{dd} \\ X_{N^* d} \\ X_{d_y d} \end{pmatrix}. \quad (9)$$

B. Cross sections for $K^- d \rightarrow \pi \Sigma n$

In this subsection, following Ref. [22], we present formulas for computing cross sections of the two-body-to-three-body reaction, $K^- d \rightarrow \pi \Sigma n$. By using the anti-symmetrized AGS amplitudes (9), the breakup amplitudes for $K^- d \rightarrow \pi \Sigma n$ are given as

$$\begin{aligned} T_{K^- d \rightarrow \pi \Sigma n}(\mathbf{q}_N, \mathbf{p}_N, \mathbf{p}_{\bar{K}}, W) &= \frac{1}{\sqrt{2}} \sum_{I,L} \\ &\times \left[\langle \pi \Sigma n | [[\pi \otimes \Sigma]_{Y_\pi} \otimes N]_{\Gamma}; I, L \rangle g_{Y_\pi}^{(I)}(q_N) \tau_{Y_\pi Y_K}^{(I)}(W - E_N(\mathbf{p}_N), \mathbf{p}_N) X_{Y_K d, L}^{(I)(I=0)}(p_N, p_{\bar{K}}, W) \right. \\ &+ \langle \pi \Sigma n | [[\pi \otimes \Sigma]_{Y_\pi} \otimes N]_{\Gamma}; I, L \rangle g_{Y_\pi}^{(I)}(q_N) \tau_{Y_\pi Y_\pi}^{(I)}(W - E_N(\mathbf{p}_N), \mathbf{p}_N) X_{Y_\pi d, L}^{(I)(I=0)}(p_N, p_{\bar{K}}, W) \\ &+ \langle \pi \Sigma n | [[\pi \otimes N]_{N^*} \otimes \Sigma]_{\Gamma}; I, L \rangle g_{N^*}^{(I)}(q_\Sigma) \tau_{N^* N^*}^{(I)}(W - E_\Sigma(\mathbf{p}_\Sigma), \mathbf{p}_\Sigma) X_{N^* d, L}^{(I)(I=0)}(p_\Sigma, p_{\bar{K}}, W) \\ &+ \left. \langle \pi \Sigma n | [[\Sigma \otimes N]_{d_y} \otimes \pi]_{\Gamma}; I, L \rangle g_{d_y}^{(I)}(q_\pi) \tau_{d_y d_y}^{(I)}(W - E_\pi(\mathbf{p}_\pi), \mathbf{p}_\pi) X_{d_y d, L}^{(I)(I=0)}(p_\pi, p_{\bar{K}}, W) \right] \\ &\times \langle [d \otimes \bar{K}]_{\Gamma'}; I=0, L | d K^- \rangle \sqrt{R_d}. \end{aligned} \quad (10)$$

Here R_d is the residue of the two-body NN propagator, $\tau_{dd}^{(I=0)}$ at the deuteron pole, with its proper binding energy, i.e., $\sqrt{R_d}$ normalizes the initial state deuteron wave function. Note again that all two-body subsystems listed in Table I, including both hyperons $Y = \Sigma$ and Λ , contribute to $T_{K^- d \rightarrow \pi \Sigma n}$ when permitted by selection rules. The following notations are used for the expressions appearing in Eq. (10):

$|ABC\rangle$: plane wave state of the three-body system;

$[[A \otimes B]_\alpha \otimes C]_{\Gamma}; I, L$: three-body system in the LS coupling scheme, with α , Γ , I , and L being the isobar quantum number, the total quantum number, the isospin of the isobar and its angular momentum relative to the spectator, respectively.

The projection $\langle ABC|[[A \otimes B]_\alpha \otimes C]_\Gamma; I, L\rangle$ involves the product of spherical harmonics and spin-isospin Clebsch-Gordan coefficients. The T matrix calculated in the isospin basis is then decomposed into the $\pi^+\Sigma^-n$, $\pi^0\Sigma^0n$, and $\pi^-\Sigma^+n$ final states using isospin CG coefficients. The momenta \mathbf{p}_π and \mathbf{p}_Σ are related to the momenta \mathbf{p}_N and \mathbf{q}_N by a Lorentz boost

$$\mathbf{p}_\pi = \mathbf{q}_N - \frac{\mathbf{p}_N}{M_{\pi\Sigma}(\mathbf{q}_N)} \left[E_\pi(\mathbf{q}_N) - \frac{\mathbf{p}_N \cdot \mathbf{q}_N}{E_{\pi\Sigma}(\mathbf{p}_N, \mathbf{q}_N) + M_{\pi\Sigma}(\mathbf{q}_N)} \right], \quad (11)$$

$$\mathbf{p}_\Sigma = -\mathbf{q}_N - \frac{\mathbf{p}_N}{M_{\pi\Sigma}(\mathbf{q}_N)} \left[E_\Sigma(\mathbf{q}_N) + \frac{\mathbf{p}_N \cdot \mathbf{q}_N}{E_{\pi\Sigma}(\mathbf{p}_N, \mathbf{q}_N) + M_{\pi\Sigma}(\mathbf{q}_N)} \right]. \quad (12)$$

With the T matrix Eq. (10) the cross sections of interest are derived as

$$\begin{aligned} \sigma(W) &= \frac{(2\pi)^4}{v} \int d^3\mathbf{p}_N d^3\mathbf{q}_N \sum_{\bar{i}f} \delta(W - E_N(\mathbf{p}_N) - E_{\pi\Sigma}(\mathbf{p}_N, \mathbf{q}_N)) |T_{K^-d \rightarrow \pi\Sigma n}(\mathbf{q}_N, \mathbf{p}_N, \mathbf{p}_{\bar{K}}, W)|^2 \\ &= (2\pi)^4 \frac{E_d E_{\bar{K}}}{W p_{\bar{K}}} \int dM_{\pi\Sigma} d\hat{\mathbf{p}}_N d\hat{\mathbf{q}}_N \frac{E_N(\mathbf{p}_N) E_\Sigma(\mathbf{p}_\Sigma) E_\pi(\mathbf{p}_\pi)}{W} p_N q_N \sum_{\bar{i}f} |T_{K^-d \rightarrow \pi\Sigma n}(\mathbf{q}_N, \mathbf{p}_N, \mathbf{p}_{\bar{K}}, W)|^2 \end{aligned} \quad (13)$$

with the initial relative velocity $v = \frac{W}{E_d E_{\bar{K}}} p_{\bar{K}}$, the $\pi\Sigma$ invariant/missing mass $M_{\pi\Sigma} = E_\pi(\mathbf{q}_N) + E_\Sigma(\mathbf{q}_N) = \sqrt{(W - E_N(\mathbf{p}_N))^2 - \mathbf{p}_N^2}$, and the K^-d total energy $W = E_{\bar{K}}(\mathbf{p}_{\bar{K}}) + E_d(\mathbf{p}_{\bar{K}}) = \sqrt{m_{\bar{K}}^2 + \mathbf{p}_{\bar{K}}^2} + \sqrt{m_d^2 + \mathbf{p}_{\bar{K}}^2}$. In the second line of Eq. (13), the momenta p_N and q_N are the on-shell momenta for given energies W and $M_{\pi\Sigma}$. Angular integrations are denoted by $\int d\hat{\mathbf{p}} \equiv \int d\cos\theta_p d\phi_p$. The differential cross sections are

$$\frac{d^2\sigma}{dM_{\pi\Sigma} d\cos\theta_{p_N}} = (2\pi)^4 \frac{E_d E_{\bar{K}}}{W p_{\bar{K}}} \int d\phi_{p_N} d\hat{\mathbf{q}}_N \frac{E_N(\mathbf{p}_N) E_\Sigma(\mathbf{p}_\Sigma) E_\pi(\mathbf{p}_\pi)}{W} p_N q_N \sum_{\bar{i}f} |T_{K^-d \rightarrow \pi\Sigma n}(\mathbf{q}_N, \mathbf{p}_N, \mathbf{p}_{\bar{K}}, W)|^2, \quad (14)$$

$$\frac{d\sigma}{dM_{\pi\Sigma}} = (2\pi)^4 \frac{E_d m_{\bar{K}}}{W p_{\bar{K}}} \int d\hat{\mathbf{p}}_N d\hat{\mathbf{q}}_N \frac{E_N(\mathbf{p}_N) E_\Sigma(\mathbf{p}_\Sigma) E_\pi(\mathbf{p}_\pi)}{W} p_N q_N \sum_{\bar{i}f} |T_{K^-d \rightarrow \pi\Sigma n}(\mathbf{q}_N, \mathbf{p}_N, \mathbf{p}_{\bar{K}}, W)|^2, \quad (15)$$

where

$$\cos\theta_{p_N} = \hat{\mathbf{p}}_N \cdot \hat{\mathbf{q}}_N. \quad (16)$$

The symbol $\sum_{\bar{i}f}$ stands as usual for averaging of initial states and sum of final states subject to conservation laws.

III. TWO-BODY INTERACTIONS

We refer back to Eq. (1) and explain the explicit forms of the meson-baryon interactions (Sec. III A) and baryon-baryon interactions (Sec. III C) used in this work. In this section spectator indices are suppressed for simplicity.

A. Meson-baryon interaction

Two models for the s -wave meson-baryon interactions used in Refs. [13, 19, 20, 22] are employed in this work. Both are derived from the leading order chiral Lagrangian (the Weinberg-Tomozawa term [54, 55]) but have different off-shell behavior. One of them is referred to as the

energy dependent (E-dep.) model [20],

$$\begin{aligned} V_{\alpha\beta}^{(I)\text{E-dep.}}(q_\alpha, q_\beta; E) \\ = -\frac{C_{\alpha\beta}^I}{32\pi^2 f_\pi^2} \frac{2E - M_\alpha - M_\beta}{\sqrt{\omega_\alpha \omega_\beta}} g_\alpha^{(I)}(q_\alpha) g_\beta^{(I)}(q_\beta). \end{aligned} \quad (17)$$

Here, $\omega_\alpha = \sqrt{q_\alpha^2 + m_\alpha^2}$ is the meson energy of the channel $\alpha = \bar{K}N, \pi\Sigma, \pi\Lambda$; m_α (M_α) is the meson (baryon) mass; $f_\pi = 92.4$ MeV is the pion decay constant; the coupling coefficients $C_{\alpha\beta}^I$ are determined by the flavor SU(3) structure constant (see Ref. [22]). The vertex factors $g_\alpha^{(I)}(q_\alpha)$ are chosen as dipole form factors with cutoff scales $\Lambda_\alpha^{(I)}$,

$$g_\alpha^{(I)}(q_\alpha) = \left(\frac{\Lambda_\alpha^{(I)2}}{\Lambda_\alpha^{(I)2} + q_\alpha^2} \right)^2.$$

The characteristic energy dependence of the meson-baryon interaction (17) is dictated by spontaneously broken chiral $SU(3)_L \times SU(3)_R$ symmetry. The corresponding Nambu-Goldstone bosons are identified with

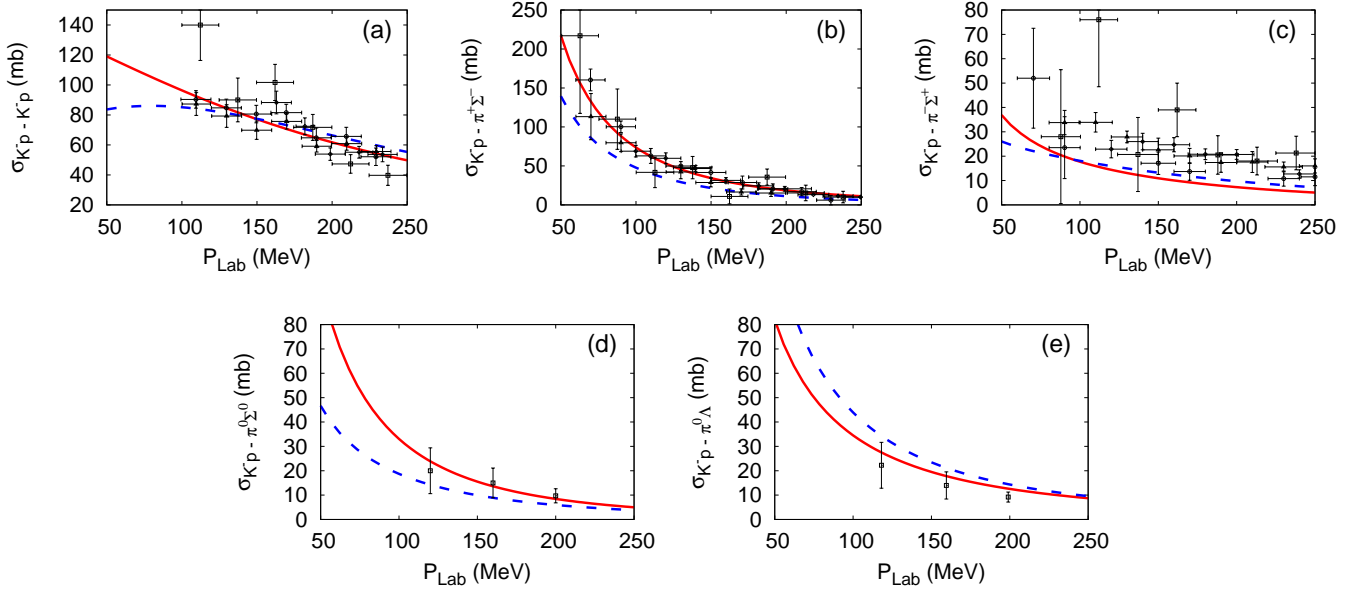


FIG. 2. (Color online) Results of the fit with the E-dep. model (solid lines) and E-indep. model (dashed lines). Total cross sections of (a) $K^-p \rightarrow K^-p$, (b) $K^-p \rightarrow \pi^+\Sigma^-$, (c) $K^-p \rightarrow \pi^-\Sigma^+$, (d) $K^-p \rightarrow \pi^0\Sigma^0$, and (e) $K^-p \rightarrow \pi^0\Lambda$. Data are from Refs. [23–27].

TABLE II. Cutoff parameters of the $\bar{K}N$ - πY interaction.

	$\Lambda_{YK}^{(I=0)}$ (MeV)	$\Lambda_{Y\pi=\pi\Sigma}^{(I=0)}$ (MeV)	$\Lambda_{YK}^{(I=1)}$ (MeV)	$\Lambda_{Y\pi=\pi\Sigma}^{(I=1)}$ (MeV)	$\Lambda_{Y\pi=\pi\Lambda}^{(I=1)}$ (MeV)
E-dep.	1100	1100	800	800	800
E-indep.	1160	1100	1100	850	1250

the pseudoscalar meson octet, and their leading s -wave couplings involve the time derivatives of the meson fields.

The other model, referred to here as the energy independent (E-indep.) model [13, 19], is obtained by fixing the two-body energy at each threshold energy, $2E = m_\alpha + M_\alpha + m_\beta + M_\beta$:

$$V_{\alpha\beta}^{(I)\text{E-indep.}}(q_\alpha, q_\beta) = -\frac{C_{\alpha\beta}^I}{32\pi^2 f_\pi^2} \frac{m_\alpha + m_\beta}{\sqrt{\omega_\alpha \omega_\beta}} g_\alpha^{(I)}(q_\alpha) g_\beta^{(I)}(q_\beta). \quad (18)$$

While this restricted model with constant couplings is not consistent with Goldstone's theorem for low-energy pseudoscalar meson interactions, it is nonetheless a prototype of phenomenological potentials that have been used in the literature, and so we discuss it here for comparison with the energy-dependent approach based on chiral $SU(3)_L \times SU(3)_R$ meson-baryon effective field theory.

The cutoff parameters for the $\bar{K}N$ - $\pi\Sigma$ - $\pi\Lambda$ systems are determined by fitting the K^-p scattering cross sections [23–27]. Results of the fit for the E-dep. and E-indep. models are presented in Fig. 2. The fitted cutoff values are listed in Table II.

The different off-shell behaviors of the two types of models leads to different analytic structure of the $\bar{K}N$ amplitudes. We find that the E-dep. model has two poles on the $\bar{K}N$ physical and $\pi\Sigma$ unphysical sheet. The behavior of the subthreshold amplitudes is similar to that obtained with the chiral $SU(3)$ dynamics [35, 36] (see Fig. 3), and the scattering length is consistent with SIDDHARTA measurement in the E-dep. model. On the other hand, the E-indep. model has a single pole corresponding to $\Lambda(1405)$. It shares this property with other phenomenological potential models. The behavior below $\bar{K}N$ threshold of the amplitudes in the E-indep. model is very different compared with that obtained from chiral $SU(3)$ dynamics (Fig. 3). In the E-indep. model, it is difficult to reproduce the K^-p scattering length in comparison with SIDDHARTA measurements although the cross sections are reproduced within experimental errors.

Table III lists the pole energies of the $\bar{K}N$ s -wave scattering amplitudes in the complex energy plane between the $\bar{K}N$ and $\pi\Sigma$ threshold energies and the K^-p scattering length. The primary purpose of this study is to clarify the influence of the subthreshold behavior of the $\bar{K}N$ interaction in the $\pi\Sigma$ spectrum.

As for the cutoff parameters of πN interactions, we

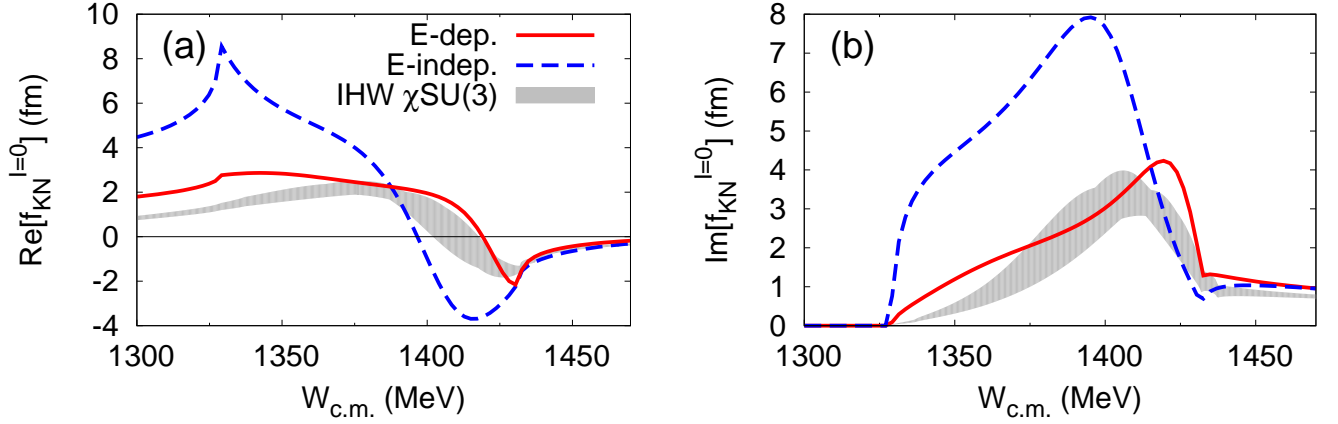


FIG. 3. (Color online) (a) Real and (b) imaginary parts of the $\bar{K}N$ amplitude in the isospin $I = 0$ channel as functions of the total $\bar{K}N$ center-of-mass energy. Solid curve: E-dep. model based on the chiral SU(3) potential (17); dashed curve: E-indep. model using the potential (18). The shaded area show for comparison the $I = 0$ $\bar{K}N$ amplitude from NLO chiral SU(3) dynamics including uncertainties as described in Ref. [36].

TABLE III. Resonance energies E_R of the $I = 0$ $\bar{K}N-\pi\Sigma$ interaction and the K^-p scattering lengths a_{K^-p} for the E-dep. and E-indep. models. The scattering length a_{K^-p} from the SIDDHARTA measurements are extracted using the improved Deser-Trueman formula [56].

	E_R (MeV)	a_{K^-p} (fm)
E-dep. model	$1428.8 - i 15.3$ $1344.0 - i 49.0$	$-0.72 + i 0.77$
E-indep. model	$1405.8 - i 25.2$	$-0.54 + i 0.46$
SIDDHARTA		$-0.65(0.10) + i 0.81(0.15)$

have determined them by fitting the S_{11} and S_{31} πN scattering lengths [57]. The resulting values are $\Lambda_{N^*}^{(I=1/2)} = \Lambda_{N^*}^{(I=3/2)} = 500$ MeV for both the E-dep. and E-indep. models.

B. Cutoff parameter dependence

Parameters of the two-body potential are the cutoffs $\Lambda_\alpha^{(I)}$, determined by fitting the $\bar{K}N$ reaction cross sections within experimental errors. Acceptable variations of these cutoffs are examined for the E-dep. model. The ranges of cutoff scales compatible with experimental errors are listed in Table IV and the corresponding fits to data are presented in Fig. 4. The resulting K^-p scattering length including uncertainties is $a_{K^-p} = -(0.72_{-0.12}^{+0.06}) + i (0.77_{-0.15}^{+0.19})$ fm, consistent with the scattering length deduced from the SIDDHARTA kaonic hydrogen measurements.

As seen in Fig. 4 one might have the impression that the $K^-p \rightarrow \pi^- \Sigma^+$ cross section is not optimally repro-

duced. On the other hand, this is a relatively small cross section with limited weight in the overall fitting procedure. By examining the dashed curves in Fig. 4, we have checked that optimizing the fit to this selected cross section does not have a significant influence on the other cross sections within uncertainties.

C. Baryon-baryon interactions

The following baryon-baryon interactions are commonly used for the E-dep. and E-indep. meson-baryon models. As for the NN interaction in 3S_1 , we take the following Yamaguchi-type two-term separable form:

$$V_{d,d}^{(I=0)}(q', q) = 4\pi C_R g_R(q') g_R(q) + 4\pi C_A g_A(q') g_A(q). \quad (19)$$

Here, C_R (C_A) is the coupling strength of the repulsive (attractive) potential. The form factors $g_{R,A}(q)$ are defined by $g_{R,A}(q) = \Lambda_{R,A}^2 / (q^2 + \Lambda_{R,A}^2)$, with $\Lambda_{R,A}$ being the cutoff parameters of the NN interactions. The coupling strengths $C_{R,A}$ and the cutoff parameters $\Lambda_{R,A}$ are determined by fitting the 3S_1 phase shifts of the Nijmegen 93 model [58] (see Fig. 5 for the result of the fit). The resulting values of the parameters are summarized in Table V. The obtained deuteron binding energy is 2.23 MeV.

As for the s -wave YN interactions, we follow the form given in Ref. [59]:

$$V_{\alpha\beta}^{(I)}(q_\alpha, q_\beta) = -4\pi \frac{C_{\alpha\beta}^{(I)}}{2\pi^2} (\mu_\alpha \mu_\beta \Lambda_\alpha^{(I)} \Lambda_\beta^{(I)})^{-1/2} \times g_\alpha^{(I)}(q_\alpha) g_\beta^{(I)}(q_\beta). \quad (20)$$

Here, μ_α is the reduced mass of the YN system; the form factor $g_\alpha^{(I)}(q_\alpha)$ is defined as $g_\alpha^{(I)}(q_\alpha) = \Lambda_\alpha^{(I)2} / (q_\alpha^2 + \Lambda_\alpha^{(I)2})$.

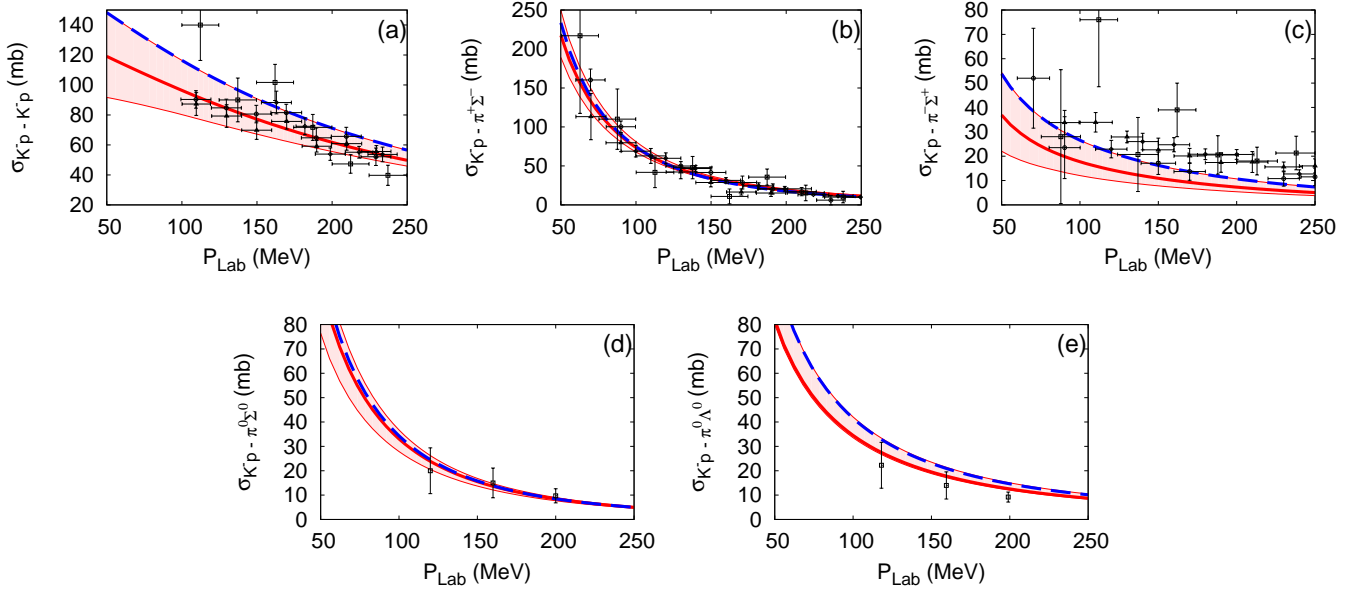


FIG. 4. (Color online) Results of the fit with the E-dep. model. Total cross sections of (a) $K^-p \rightarrow K^-p$, (b) $K^-p \rightarrow \pi^+\Sigma^-$, (c) $K^-p \rightarrow \pi^-\Sigma^+$, (d) $K^-p \rightarrow \pi^0\Sigma^0$, and (e) $K^-p \rightarrow \pi^0\Lambda$. Data are from Refs. [23–27]. The shaded areas reflect variations of the cutoff $\Lambda_\alpha^{(I)}$ as listed in Table IV. In (c) the dashed curve indicates the best consistent fit to the $K^-p \rightarrow \pi^-\Sigma^+$ cross section. Its implication for the other cross sections is shown by the dashed curves in subfigures (a), (b), (d), and (e).

TABLE IV. Ranges of cutoff parameters of the $\bar{K}N$ - πY interaction compatible with experimental errors.

	$\Lambda_{YK}^{(I=0)}$ (MeV)	$\Lambda_{Y\pi=\pi\Sigma}^{(I=0)}$ (MeV)	$\Lambda_{YK}^{(I=1)}$ (MeV)	$\Lambda_{Y\pi=\pi\Sigma}^{(I=1)}$ (MeV)	$\Lambda_{Y\pi=\pi\Lambda}^{(I=1)}$ (MeV)
E-dep.	1070-1170	1070-1170	790-900	790-900	790-900

TABLE V. Parameters of the NN interaction in 3S_1 .

Λ_R (MeV)	Λ_A (MeV)	C_R (MeV fm ³)	C_A (MeV fm ³)
1350	321	1.41	-5.59

TABLE VI. Coupling constants of the YN interactions.

$C_{\Sigma N \Sigma N}^{(I=1/2)}$	$C_{\Sigma N \Lambda N}^{(I=1/2)}$	$C_{\Lambda N \Lambda N}^{(I=1/2)}$	$C_{\Sigma N \Sigma N}^{(I=3/2)}$
1.51	0.40	1.08	-1.11

The coupling constants $C_{\alpha\beta}^{(I)}$ and the cutoff parameters $\Lambda_\alpha^{(I)}$ are determined by fitting the 3S_1 phase shifts of the Jülich'04 model [60]. The resulting values of the coupling constants $C_{\alpha\beta}^{(I)}$ are summarized in Table VI. The cutoff parameters $\Lambda_\alpha^{(I)}$ are $\Lambda_{\Sigma N}^{(I=1/2)} = 261$ MeV, $\Lambda_{\Sigma N}^{(I=3/2)} = 540$ MeV, and $\Lambda_{\Lambda N}^{(I=1/2)} = 285$ MeV.

IV. RESULTS AND DISCUSSION

A. Differential cross section of the $K^-d \rightarrow \pi\Sigma n$ reaction

We proceed now to investigate the dependence of the differential cross section, $d\sigma/dM_{\pi\Sigma}$ of Eq. (15), as a function of the invariant mass of the final $\pi\Sigma$ state. Results for the different $\pi\Sigma$ charge combinations, $K^-d \rightarrow \pi^+\Sigma^-n$, $K^-d \rightarrow \pi^-\Sigma^+n$, and $K^-d \rightarrow \pi^0\Sigma^0n$ are shown in Fig. 6 (a) and (b) for the E-dep. and E-indep. models, respectively, whereby the isospin basis states have been decomposed into charge basis states using Clebsch-Gordan coefficients. In view of the planned J-PARC experiment, the initial K^- momentum is chosen as $p_K^{\text{lab}} = 1$ GeV/c, corresponding to the K^-d total energy $\sqrt{s} = W = 2817$ MeV.

The differential cross section is an order of magnitude smaller than that calculated by assuming a two-step process [48–51]. Well-defined maxima are found at $M_{\pi\Sigma} \sim 1420$ -1430 MeV for the E-dep. model in all

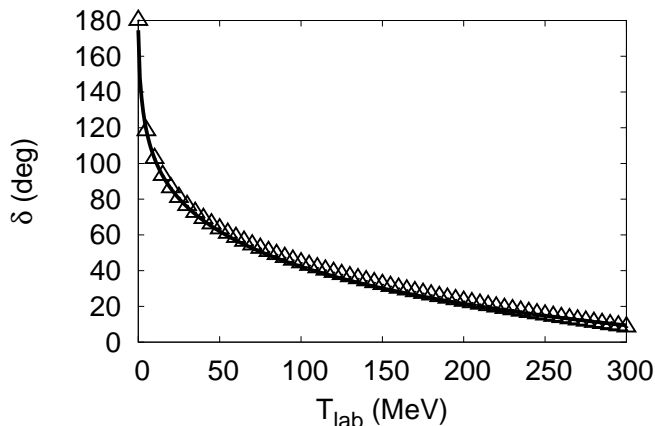


FIG. 5. Phase shifts of the NN scattering in the 3S_1 channel. The solid line shows the phase shift with our model, and the triangles show the phase shifts with the model of Ref. [58].

charge combinations of $\pi\Sigma$ in the final state ². The positions of the peak structures are close to the calculated quasi bound $\bar{K}N$ pole position ($M_{\pi\Sigma} \sim 1429$ MeV). In the E-dep. model, the second pole with its large width, $\Gamma \simeq 98$ MeV, barely affects the differential cross section. On the other hand, no resonance structure is seen for the E-indep. model. The magnitude of the differential cross section and the interference patterns with backgrounds are evidently different for the E-dep. and E-indep. models. This suggests that the $K^-d \rightarrow \pi\Sigma n$ reaction can indeed provide significant information on the $\bar{K}N$ - πY subsystem.

Next, we show the contributions of each reaction process to the differential cross section (Fig. 7). As can be seen in Eq. (10), the reaction dynamics involves the quasi-two-body processes characterized by the amplitudes $X_{Y_K,d}$, $X_{Y_\pi,d}$, $X_{N^*,d}$, and $X_{d_y,d}$. The $X_{Y_K,d}$ amplitude which contains the $\bar{K}N \rightarrow \pi\Sigma$ final state interaction turns out to be the dominant contribution to the cross section. The contribution from $X_{d_y,d}$ modifies the cross section for $\pi^-\Sigma^+n$ and $\pi^0\Sigma^0n$ final states, while its influence is small for the $\pi^+\Sigma^-n$ final state. This is because the $X_{d_y,d}^{(I=1/2)(I=0)}$ component has Clebsch-Gordan coefficients which cancel for $\pi^+\Sigma^-n$ final state.

B. Partial waves and angular dependence of the reaction

Consider now the contributions from each partial wave component with orbital angular momentum L to the

differential cross section for E-dep. model. The solid curve in Fig. 8 show the results with the total orbital angular momentum summed up to $L = 10$, which correspond to those shown in Fig. 6 (a), respectively. The decomposition into angular momentum contributions with $L = 0, 1, 2$, and 3 displayed in this figure demonstrates the convergence of the partial wave expansion. The large incident K^- energy implies that there are sizable contributions with $L \neq 0$. The s - and d -wave components dominate in the region below $\bar{K}N$ threshold. Around the threshold the p -wave component also becomes important for the $\pi^+\Sigma^-n$ and $\pi^-\Sigma^+n$ channels.

It is instructive to investigate the angular dependence of the double differential cross section, $d^2\sigma/dM_{\pi\Sigma}d\cos\theta_{p_N}$ defined in Eq. (14). In Fig. 9 (Fig. 10), we present the double differential cross section for neutron scattering angles (a) $\theta_{p_N} = 0^\circ$, (b) $\theta_{p_N} = 90^\circ$, and (c) $\theta_{p_N} = 180^\circ$ for E-dep. model (E-indep. model). Here θ_{p_N} is the neutron scattering angle in the center-of-mass frame. At $\theta_{p_N} = 0^\circ$ one finds a strong dependence on the final state. The $\bar{K}N$ threshold cusp effect is enhanced in the $\pi^+\Sigma^-n$ and $\pi^-\Sigma^+n$ channels. The detailed channel dependence is closely related to the interference of the isospin $I = 0$ and $I = 1$ components of the $\pi\Sigma$ in the final state. The forward $K^-d \rightarrow \pi\Sigma n$ reaction thus provides information on the $\bar{K}N$ - πY interaction not only in the $I = 0$ but also in $I = 1$ channel.

At $\theta_{p_N} = 90^\circ$ the differential cross section is strongly suppressed in both the E-dep. and E-indep. models. It remains relatively flat at $\theta_{p_N} = 180^\circ$. Clearly, the interesting physics information is expected to be observable primarily with neutrons produced in forward direction. In the actual experiment the neutron will be detected in a forward cone around $\theta_{p_N} = 0^\circ$. We have checked that the differential cross section integrated over an angle interval from $\theta_{p_N} = 0^\circ$ to 30° does not change much from the pattern seen at $\theta_{p_N} = 0^\circ$.

C. Cross sections above the $\bar{K}N$ threshold energy and cutoff dependence

While the primary focus in this study is on the $\bar{K}N$ subthreshold region and the two-body $\bar{K}N$ - πY dynamics governing the $\Lambda(1405)$ formation in the $\bar{K}NN$ three-body system, it is also instructive to explore $\pi\Sigma$ invariant mass spectra above $\bar{K}N$ threshold in $K^-d \rightarrow (\pi\Sigma)n$. In fact our calculation (see Fig. 11) yields pronounced structures, especially for the charged channels ($\pi^+\Sigma^-$ and $\pi^-\Sigma^+$), in the angle-integrated differential cross section. These structures are qualitatively different in the E-dep. and E-indep. approaches.

The $K^-d \rightarrow (\pi\Sigma)n$ double differential cross section with the neutron emitted in forward direction is of special interest (see Fig. 12). Our three-body calculations predict a strongly developed maximum around $M_{\pi\Sigma} = 1.45$ GeV for both the E-dep. and the E-indep. models, a feature that should be well observable. A less pro-

² The difference among the spectra in the charge basis is due to the interference effect with the $I = 1$ amplitude [64].

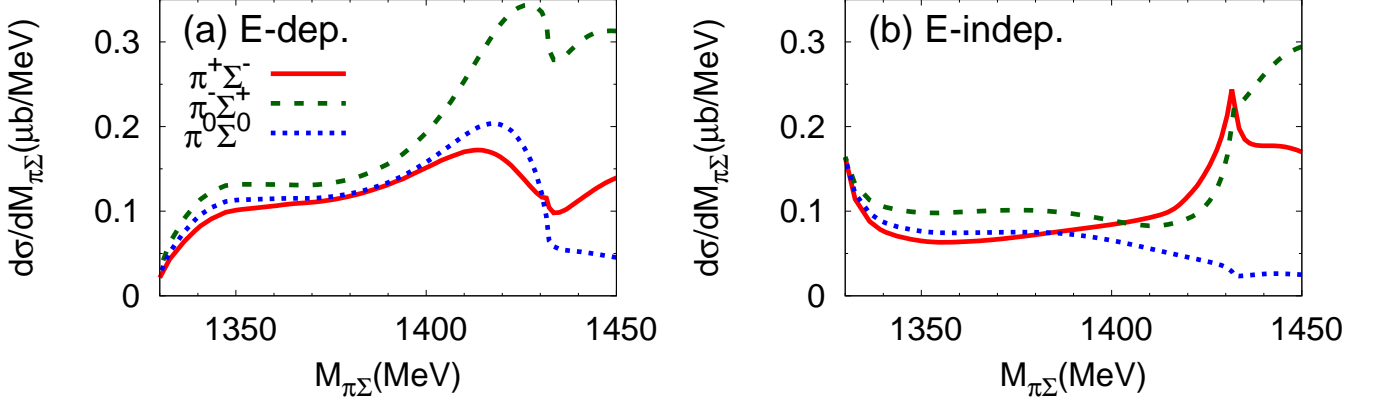


FIG. 6. (Color online) Differential cross sections $d\sigma/dM_{\pi\Sigma}$ for $K^-d \rightarrow \pi\Sigma n$. The initial kaon momentum is set to $p_{\text{lab}} = 1$ GeV. (a) E-dep. model; (b) E-indep. model. Solid curves: $\pi^+\Sigma^-n$; dashed curves: $\pi^-\Sigma^+n$; dotted curves: $\pi^0\Sigma^0n$ in the final state, respectively.

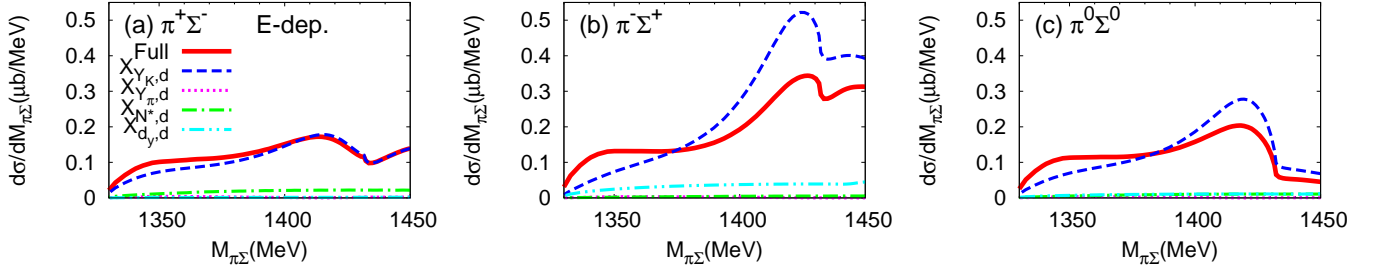


FIG. 7. (Color online) Contributions from each two-body reaction process to the $K^-d \rightarrow \pi\Sigma n$ differential cross section $d\sigma/dM_{\pi\Sigma}$ using the E-dep. model. (a) $\pi^+\Sigma^-n$; (b) $\pi^-\Sigma^+n$; (c) $\pi^0\Sigma^0n$ in the final state. The solid curve represents the summation of all reaction processes of Eq. (10); dashed curve: $X_{Y_{K,d}}$ component; dotted curve: $X_{Y_{\pi,d}}$ component; dotted-dotted curve: $X_{N^*,d}$ component; dashed-two-dotted curve: $X_{d_{y,d}}$ component, respectively. The initial kaon momentum is set to $p_{\text{lab}} = 1$ GeV.

nounced effect is seen in the $K^-d \rightarrow \pi^+\Sigma^-n$ channel which requires both charge exchange and strangeness exchange mechanisms.

The appearance of the prominent maximum in $d^2\sigma/dM_{\pi\Sigma}d\cos\theta_{p_N}$ around $M_{\pi\Sigma} = 1.45$ GeV can be traced to a combination of subtle three-body mechanisms in the coupled K^-pn - $\pi\Sigma n$ system: the nucleon exchange process between the incident K^- and the deuteron, with a propagating $\bar{K}N$ pair and a spectator nucleon, and subsequent $\bar{K}N$ exchange leading to the final $\pi\Sigma$ and neutron. The momentum matching between these two basic processes in the three-body system produces the pronounced enhancement in the $(\pi^-\Sigma^+)n$ channel about 20 MeV above $\bar{K}N$ threshold.

The appearance of such a structure in $d^2\sigma/dM_{\pi\Sigma}d\cos\theta_{p_N}$ raises of course the question of model dependence and sensitivity to cutoff variations in the two-body amplitudes. This cutoff dependence turns out indeed to be stronger in the three-body

system with its off-shell dynamics, as compared to the two-body subsystems. In order to examine this issue, we have performed calculations of the $K^-d \rightarrow \pi\Sigma n$ differential cross sections using the acceptable range of cutoff scales at the two-body vertices discussed previously and listed in Table IV. This leads to the theoretical uncertainty bands displayed in Fig. 13 for $d\sigma/dM_{\pi\Sigma}$ and in Fig. 14 for the double differential cross section with forward-emitted neutron, both taken at an incident K^- momentum $p_{\text{lab}} = 1$ GeV. In particular, we have examined the influence of using the optimized cross section for $K^-p \rightarrow \pi^-\Sigma^+$ while maintaining the other cross sections well reproduced within uncertainties (compare the solid and dashed curves in Figs. 13 and 14). While the absolute magnitudes of the differential cross sections are indeed subject to uncertainties, the structural patterns of the forward double differential cross sections for $\pi^-\Sigma^+$ and $\pi^+\Sigma^-$ final states remains quite stable with respect to cutoff variations, with the

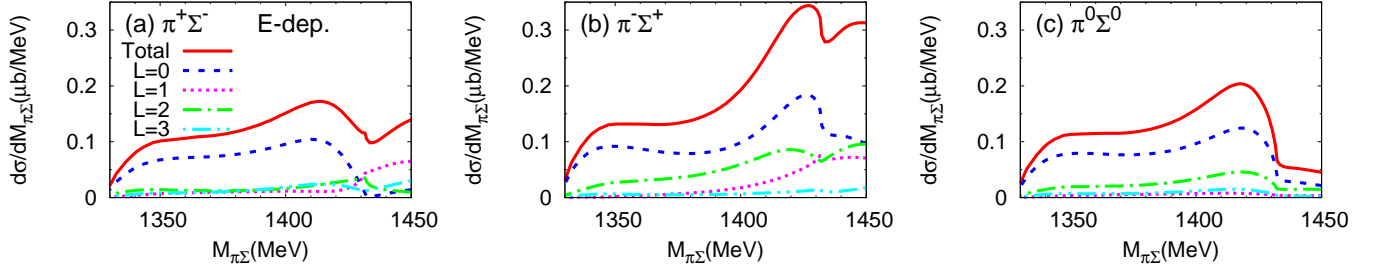


FIG. 8. (Color online) Contributions of partial wave components to the differential cross section $d\sigma/dM_{\pi\Sigma}$ for the E-dep. model. (a) $\pi^+\Sigma^-n$; (b) $\pi^-\Sigma^+n$; (c) $\pi^0\Sigma^0n$ in the final state. The solid curve represents the summation of total orbital angular momentum $L = 0$ to 10. The dashed curve represents the $L = 0$ component. The dotted curve represents the $L = 1$ component. The dashed-dotted curve represents the $L = 2$ component. The dashed-two-dotted curve represents the $L = 3$ component. The contribution from $L \geq 4$ components which we omit is small. The initial kaon momentum is set to $p_{\text{lab}} = 1$ GeV.

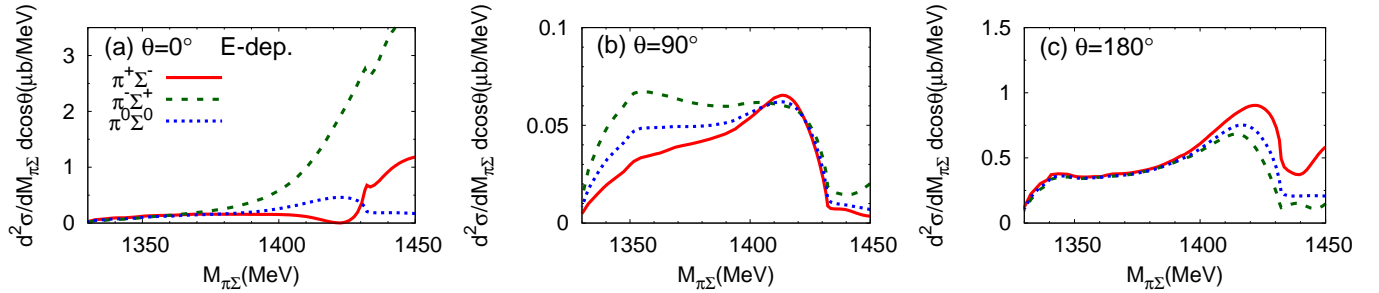


FIG. 9. (Color online) Angular dependence of the double differential cross sections $d^2\sigma/dM_{\pi\Sigma}d\cos\theta_{p_N}$ for the E-dep. model. (a) $\theta_{p_N} = 0^\circ$; (b) $\theta_{p_N} = 90^\circ$; (c) $\theta_{p_N} = 180^\circ$, respectively. Here θ_{p_N} is scattering angle of the neutron in the center-of-mass frame. The illustration of curves and the initial kaon momentum are the same as those in Fig. 6.

exception of the neutral ($\pi^0\Sigma^0$) combination for which no prediction is possible.

At the same time as this genuine three-body dynamical structure in the $\pi^-\Sigma^+n$ final state appears around $M_{\pi\Sigma} \sim 1450$ MeV, it is quite remarkable that $d^2\sigma/dM_{\pi\Sigma}d\cos\theta_{p_N}$ with forward neutrons does not display a $\Lambda(1405)$ signal any more (whereas it is still visible in the angle-integrated $d\sigma/dM_{\pi\Sigma}$ for $K^-d \rightarrow \pi^-\Sigma^+n$). This is a consequence of interferences of three-body mechanisms in $I = 0$ and $I = 1$ amplitudes which screen the $\bar{K}N$ pole contribution.

V. SUMMARY

Within the framework of the coupled-channels AGS equations, we have investigated how the signature of the $\Lambda(1405)$ appears in differential cross sections of $K^-d \rightarrow \pi\Sigma n$ reactions. Two types of meson-baryon interactions, the E-dep. and E-indep. models, have been considered to illustrate how the difference of the subthreshold behaviors translates into the $\pi\Sigma n$ spectra. The E-dep. approach is generally favored because of its foundation in chiral $SU(3)$ effective field theory.

Characteristic structures reflecting the formation and dynamics of the $\Lambda(1405)$ in the $\bar{K}NN-\pi\Sigma n$ three-body system are found in differential cross section as a function of the $\pi\Sigma$ invariant mass. By comparison of results using E-dep. and E-indep. models, it may be possible to discriminate between these two approaches, especially in comparison with separately measured $\pi^-\Sigma^+$ and $\pi^+\Sigma^-$ invariant mass spectra. Of particular interest in this context are double differential cross sections with detection of the emitted neutron in forward directions, to be measured in a forthcoming experiment at J-PARC. Detailed final state channel dependence originates from the interference of $I = 0$ and $I = 1$ components of the final $\pi\Sigma$ states, providing important information not only on the $I = 0$ but also the $I = 1$ $\bar{K}N-\pi\Sigma$ interactions.

Three-body dynamics in the coupled $K^-pn-\pi\Sigma n$ system is predicted to generate a pronounced maximum in the $K^-d \rightarrow \pi^-\Sigma^+n$ double-differential cross section with a forward-emitted neutron at a $\pi\Sigma$ invariant mass $M_{\pi\Sigma} \simeq 1.45$ GeV. Further detailed studies exploring this structure are under way.

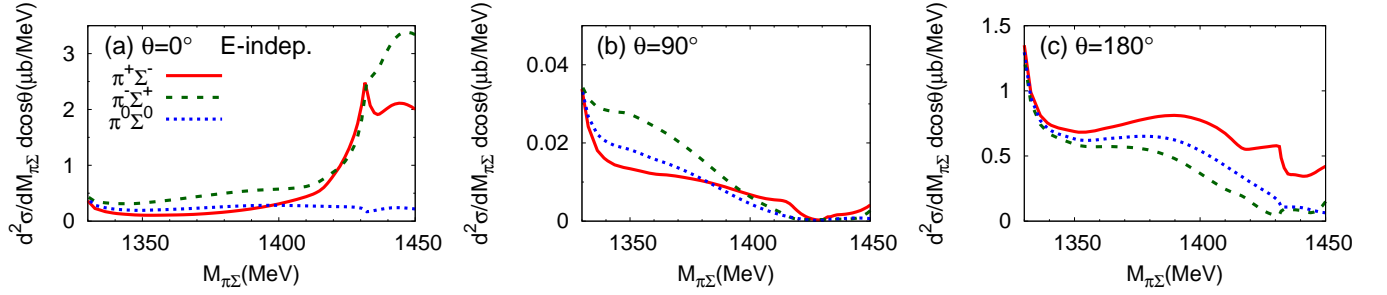


FIG. 10. (Color online) Angular dependence of the double differential cross sections $d^2\sigma/dM_{\pi\Sigma}d\cos\theta_{pN}$ for the E-indep. model. (a) $\theta_{pN} = 0^\circ$; (b) $\theta_{pN} = 90^\circ$; (c) $\theta_{pN} = 180^\circ$. The illustration of curves and the initial kaon momentum are the same as those in Fig. 6.

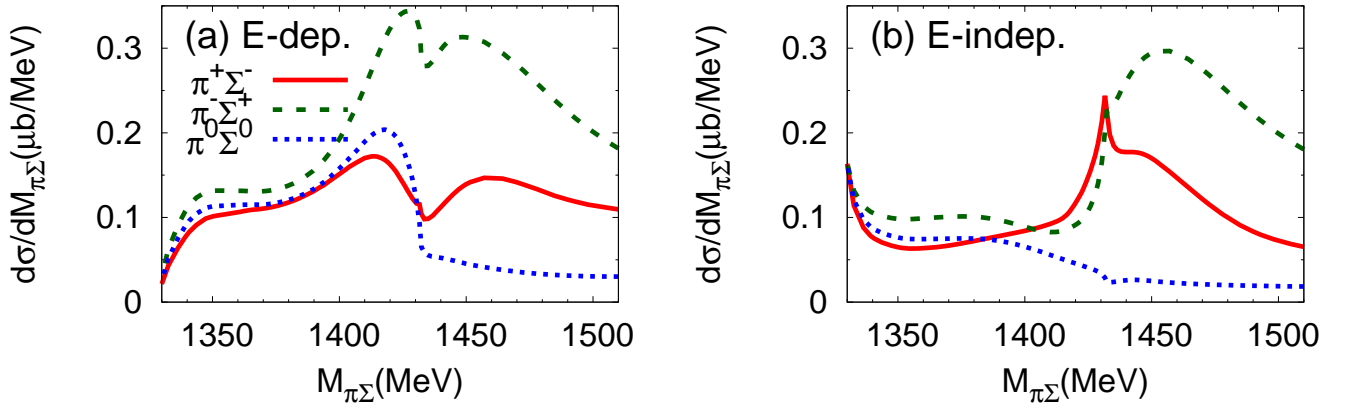


FIG. 11. (Color online) Differential cross sections $d\sigma/dM_{\pi\Sigma}$ for $K^-d \rightarrow \pi\Sigma n$. (a) The E-dep. model; (b) the E-indep. model. The illustration of curves and the initial kaon momentum are the same as those in Fig. 6.

ACKNOWLEDGMENTS

The authors thank H. Noumi and A. Hosaka for helpful comments and discussions. The numerical calculation has been performed on a supercomputer (NEC SX8R) at the Research Center for Nuclear Physics, Osaka University. This work was partly supported by the Grants-

in-Aid for Scientific Research on Innovative Areas from MEXT (Grant No. 2404:24105008), by RIKEN Junior Research Associate Program, by RIKEN iTHES Project, by the Yukawa International Program for Quark-Hadron Sciences (YIPQS), by JSPS KAKENHI Grants Nos. 23224006, 24740152 and 25800170, and by DFG through CRC 110.

-
- [1] R. Dalitz and S. Tuan, Phys. Rev. Lett. **2**, 425 (1959).
 - [2] R. Dalitz and S. Tuan, Ann. Phys. (NY) **10**, 307 (1960).
 - [3] Y. Akaishi and T. Yamazaki, Phys. Rev. **C65**, 044005 (2002).
 - [4] N. V. Shevchenko, Phys. Rev. **C85**, 034001 (2012), arXiv:1103.4974 [nucl-th].
 - [5] N. Kaiser, P. Siegel, and W. Weise, Nucl. Phys. **A594**, 325 (1995), arXiv:nucl-th/9505043 [nucl-th].
 - [6] E. Oset and A. Ramos, Nucl. Phys. **A635**, 99 (1998), arXiv:nucl-th/9711022 [nucl-th].
 - [7] J. Oller and U. G. Meissner, Phys. Lett. **B500**, 263 (2001), arXiv:hep-ph/0011146 [hep-ph].
 - [8] T. Hyodo and D. Jido, Prog. Part. Nucl. Phys. **67**, 55 (2012), arXiv:1104.4474 [nucl-th].
 - [9] T. Hyodo and W. Weise, Phys. Rev. **C77**, 035204 (2008), arXiv:0712.1613 [nucl-th].
 - [10] D. Jido, J. Oller, E. Oset, A. Ramos, and U. Meissner, Nucl. Phys. **A725**, 181 (2003), arXiv:nucl-th/0303062 [nucl-th].
 - [11] T. Yamazaki and Y. Akaishi, Phys. Lett. **B535**, 70 (2002).
 - [12] N. V. Shevchenko, A. Gal, and J. Mares, Phys. Rev. Lett.

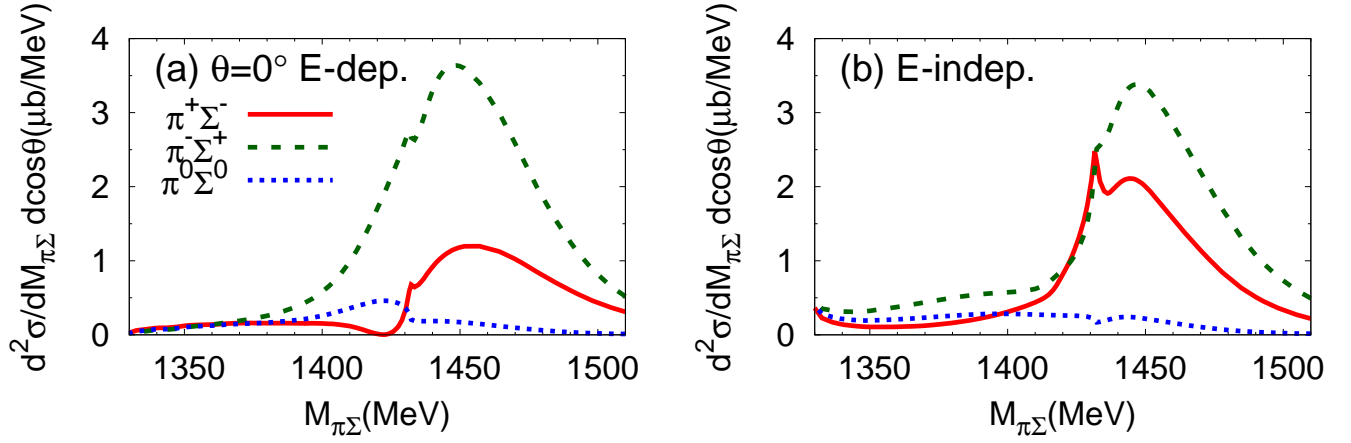


FIG. 12. (Color online) Double differential cross sections $d^2\sigma/dM_{\pi\Sigma}d\cos\theta_{pN}$ for $K^-d \rightarrow \pi\Sigma n$ with the neutron emitted in forward direction, $\theta_{pN} = 0^\circ$. (a) The E-dep. model; (b) the E-indep. model. The illustration of curves are the same as in Fig. 6. The incident K^- momentum is $p_{\text{lab}} = 1$ GeV.

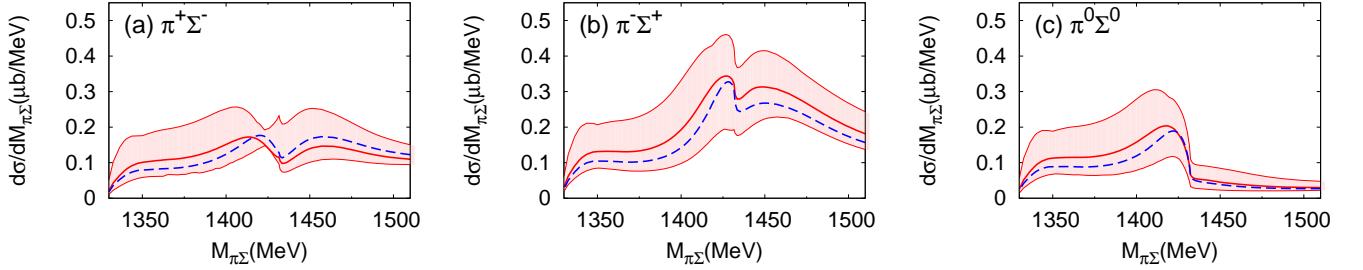


FIG. 13. (Color online) Uncertainty bands reflecting cutoff parameter dependence of the differential cross section $d\sigma/dM_{\pi\Sigma}$ for the E-dep. model. (a) $\pi^+\Sigma^-n$; (b) $\pi^-\Sigma^+n$; (c) $\pi^0\Sigma^0n$ in the final state. The initial kaon momentum is set to $p_{\text{lab}} = 1$ GeV. The dashed curves refer to the choice of “optimized” fit to the $K^-p \rightarrow \pi^-\Sigma^+$ cross section in Fig. 4.

- 98, 082301 (2007), arXiv:nucl-th/0610022 [nucl-th].
- [13] Y. Ikeda and T. Sato, Phys. Rev. **C76**, 035203 (2007), arXiv:0704.1978 [nucl-th].
- [14] N. V. Shevchenko, A. Gal, J. Mares, and J. Revai, Phys. Rev. **C76**, 044004 (2007), arXiv:0706.4393 [nucl-th].
- [15] T. Yamazaki and Y. Akaishi, Phys. Rev. **C76**, 045201 (2007), arXiv:0709.0630 [nucl-th].
- [16] A. Dote, T. Hyodo, and W. Weise, Nucl. Phys. **A804**, 197 (2008), arXiv:0802.0238 [nucl-th].
- [17] A. Dote, T. Hyodo, and W. Weise, Phys. Rev. **C79**, 014003 (2009), arXiv:0806.4917 [nucl-th].
- [18] S. Wycech and A. M. Green, Phys. Rev. **C79**, 014001 (2009), arXiv:0808.3329 [nucl-th].
- [19] Y. Ikeda and T. Sato, Phys. Rev. **C79**, 035201 (2009), arXiv:0809.1285 [nucl-th].
- [20] Y. Ikeda, H. Kamano, and T. Sato, Prog. Theor. Phys. **124**, 533 (2010), arXiv:1004.4877 [nucl-th].
- [21] N. Barnea, A. Gal, and E. Liverts, Phys. Lett. **B712**, 132 (2012), arXiv:1203.5234 [nucl-th].
- [22] S. Ohnishi, Y. Ikeda, H. Kamano, and T. Sato, Phys. Rev. **C88**, 025204 (2013), arXiv:1302.2301 [nucl-th].
- [23] W. E. Humphrey and R. R. Ross, Phys. Rev. **127**, 1305 (1962).
- [24] M. Sakitt, T. Day, R. Glasser, N. Seeman, J. Friedman, et al., Phys. Rev. **139**, B719 (1965).
- [25] J. Kim, Phys. Rev. Lett. **14**, 29 (1965).
- [26] W. Kittel, G. Otter, and I. Wacek, Phys. Lett. **21**, 349 (1966).
- [27] D. Evans, J. Major, E. Rondio, J. A. Zakrzewski, J. Conboy, et al., J. Phys. **G9**, 885 (1983).
- [28] D. Tovee, D. Davis, J. Simonovic, G. Bohm, J. Klabuhn, et al., Nucl. Phys. **B33**, 493 (1971).
- [29] R. Nowak, J. Armstrong, D. Davis, D. Miller, D. Tovee, et al., Nucl. Phys. **B139**, 61 (1978).
- [30] M. Iwasaki, R. Hayano, T. Ito, S. Nakamura, T. Terada, et al., Phys. Rev. Lett. **78**, 3067 (1997).
- [31] T. Ito, R. Hayano, S. Nakamura, T. Terada, M. Iwasaki, et al., Phys. Rev. **C58**, 2366 (1998).
- [32] G. Beer et al. (DEAR Collaboration), Phys. Rev. Lett. **94**, 212302 (2005).
- [33] M. Bazzi, G. Beer, L. Bombelli, A. Bragadireanu, M. Cargnelli, et al., Phys. Lett. **B704**, 113 (2011), cl-th].

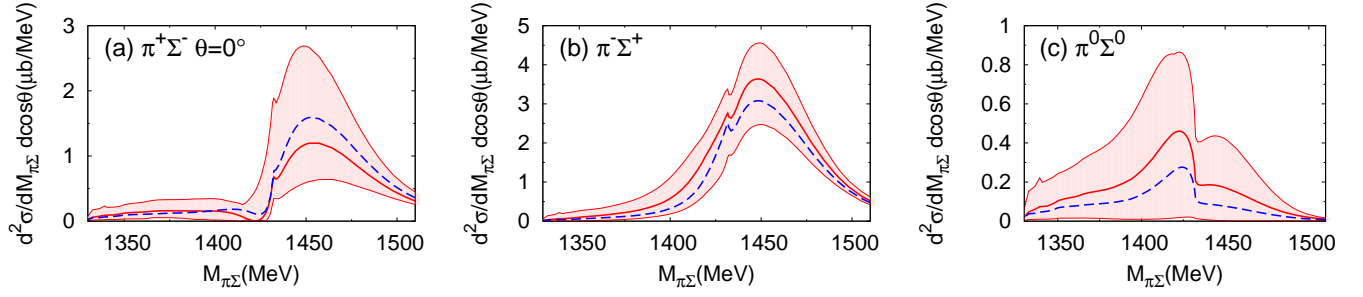


FIG. 14. (Color online) Uncertainty bands reflecting cutoff parameter dependence of the double differential cross section $d^2\sigma/dM_{\pi\Sigma}d\cos\theta_{p_N}$ for the E-dep. model, with neutrons emitted in forward direction. (a) $\pi^+\Sigma^-n$; (b) $\pi^-\Sigma^+n$; (c) $\pi^0\Sigma^0n$ in the final state. The initial kaon momentum is set to $p_{\text{lab}} = 1$ GeV. The dashed curves refer to the choice of “optimized” fit to the $K^-p \rightarrow \pi^-\Sigma^+$ cross section in Fig. 4.

- arXiv:1105.3090 [nucl-ex].
- [34] M. Bazzi, G. Beer, L. Bombelli, A. Bragadireanu, M. Cargnelli, *et al.*, Nucl.Phys. **A881**, 88 (2012), arXiv:1201.4635 [nucl-ex].
 - [35] Y. Ikeda, T. Hyodo, and W. Weise, Phys. Lett. **B706**, 63 (2011), arXiv:1109.3005 [nucl-th].
 - [36] Y. Ikeda, T. Hyodo, and W. Weise, Nucl. Phys. **A881**, 98 (2012), arXiv:1201.6549 [nucl-th].
 - [37] J. Ahn (LEPS Collaboration), Nucl.Phys. **A721**, 715 (2003).
 - [38] M. Niiyama, H. Fujimura, D. Ahn, J. Ahn, S. Ajimura, *et al.*, Phys. Rev. **C78**, 035202 (2008), arXiv:0805.4051 [hep-ex].
 - [39] K. Moriya *et al.* (CLAS Collaboration), Phys. Rev. **C87**, 035206 (2013), arXiv:1301.5000 [nucl-ex].
 - [40] K. Moriya *et al.* (CLAS Collaboration), Phys. Rev. **C88**, 045201 (2013), arXiv:1305.6776 [nucl-ex].
 - [41] G. Agakishiev *et al.* (HADES Collaboration), Phys.Rev. **C87**, 025201 (2013), arXiv:1208.0205 [nucl-ex].
 - [42] L. Roca and E. Oset, Phys. Rev. **C87**, 055201 (2013), arXiv:1301.5741 [nucl-th].
 - [43] L. Roca and E. Oset, Phys. Rev. **C88**, 055206 (2013), arXiv:1307.5752 [nucl-th].
 - [44] Z.-H. Guo and J. A. Oller, Phys. Rev. **C87**, 035202 (2013), arXiv:1210.3485 [hep-ph].
 - [45] M. Mai and U.-G. Meissner, Eur. Phys. J. **A51**, 30 (2015), arXiv:1411.7884 [hep-ph].
 - [46] O. Braun, H. Grimm, V. Hepp, H. Strobele, C. Thol, *et al.*, Nucl. Phys. **B129**, 1 (1977).
 - [47] H. Noumi *et al.*, J-PARC proposal E31, http://j-parc.jp/researcher/Hadron/en/pac_0907/pdf/Noumi.pdf (2009).
 - [48] D. Jido, E. Oset, and T. Sekihara, Eur. Phys. J. **A42**, 257 (2009), arXiv:0904.3410 [nucl-th].
 - [49] K. Miyagawa and J. Haidenbauer, Phys. Rev. **C85**, 065201 (2012), arXiv:1202.4272 [nucl-th].
 - [50] D. Jido, E. Oset, and T. Sekihara, Eur. Phys. J. **A49**, 95 (2013), arXiv:1207.5350 [nucl-th].
 - [51] J. Yamagata-Sekihara, T. Sekihara, and D. Jido, Prog. Theor. Exp. Phys. **2013**, 043D02 (2013), arXiv:1210.6108 [nucl-th].
 - [52] R. D. Amado, Phys. Rev. **132**, 485 (1963).
 - [53] E. Alt, P. Grassberger, and W. Sandhas, Nucl.Phys. **B2**, 167 (1967).
 - [54] S. Weinberg, Phys. Rev. Lett. **17**, 616 (1966).
 - [55] Y. Tomozawa, Nuovo Cimento **A46**, 707 (1966).
 - [56] U. G. Meissner, U. Raha, and A. Rusetsky, Eur. Phys. J. **C35**, 349 (2004), arXiv:hep-ph/0402261 [hep-ph].
 - [57] H. Schroder, A. Badertscher, P. Goudsmit, M. Janousch, H. Leisi, *et al.*, Phys.Lett. **B469**, 25 (1999).
 - [58] V. G. J. Stoks, R. A. M. Klomp, C. P. F. Terheggen, and J. J. de Swart, Phys.Rev. **C49**, 2950 (1994), arXiv:nucl-th/9406039 [nucl-th].
 - [59] M. Torres, R. Dalitz, and A. Deloff, Phys.Lett. **B174**, 213 (1986).
 - [60] J. Haidenbauer and Ulf.-G. Meissner, Phys. Rev. **C72**, 044005 (2005), arXiv:nucl-th/0506019 [nucl-th].
 - [61] T. H. Tan, Phys. Rev. **D7**, 600 (1973).
 - [62] D. Jido, E. Oset, and T. Sekihara, Eur. Phys. J. **A47**, 42 (2011), arXiv:1008.4423 [nucl-th].
 - [63] J. Revai, Few Body Syst. **54**, 1865 (2013), arXiv:1203.1813 [nucl-th].
 - [64] J. Nacher, E. Oset, H. Toki, and A. Ramos, Phys.Lett. **B455**, 55 (1999), arXiv:nucl-th/9812055 [nucl-th].